Polymer Testing 70 (2018) 348–362

Contents lists available at ScienceDirect

Polymer Testing

journal homepage: www.elsevier.com/locate/polytest

Material Properties

Quasi-static and dynamic mechanical behavior of transparent graft-interpenetrating polymer networks (graft-IPNs)

Balamurugan M. Sundaram[a], Ricardo B. Mendez[b], Maria L. Auad[b], Hareesh V. Tippur[a,*]

[a] Department of Mechanical Engineering, Auburn University, AL, 36849, USA
[b] Department of Chemical Engineering, Auburn University, AL, 36849, USA

ARTICLE INFO

Keywords:
Interpenetrating polymer networks
Transparent armor
Stress-strain behavior
Quasi-static and dynamic fracture
Digital image correlation

ABSTRACT

Mechanical characterization of transparent graft Interpenetrating Polymer Networks or graft-IPNs based on polyurethane and acrylic copolymer are reported under both quasi-static and dynamic loading conditions. This study builds on an earlier work detailing the synthesis of the graft-IPNs [1]. Optically transparent graft-IPNs were synthesized using elastomeric polyurethane (PU) phase and stiff acrylate-base copolymer (CoP) phase. The ratios of CoP:PU were varied from 90:10 up to 60:40 by weight. Two grades of graft-IPNs were synthesized by using 650 g mol^{-1} and 1400 g mol^{-1} poly (tetramethylene ether) glycol (PTMG) during synthesis to study the molecular weight effect. Quasi-static tensile and fracture tests as well as dynamic fracture tests were performed. The dynamic fracture tests were carried out at high strain rate using a modified-Hopkinson pressure bar in conjunction with an optical technique called Digital Gradient Sensing (DGS) and ultrahigh-speed photography. Quasi-static tests indicate significant enhancements in crack initiation toughness and change in failure mode (brittle to ductile) when the constituents were varied. Enhancements in crack inititation toughness were also observed under dynamic loading. These results were further compared with those for commercial poly (methyl methacrylate) (PMMA) and polycarbonate (PC) sheet stock. Further improvement in fracture properties were observed under quasi-static loading conditions with increase in molecular weight of PTMG. The relatively high values of fracture toughness obtained for graft-IPNs is attributed to the crosslinks generated between the CoP and PU networks.

1. Introduction

Optically transparent structural materials made from polymers or their blends are suitable for both civilian and military applications such as safety enclosures, aircraft canopies, protective eyewear, automotive windows and helmet visors etc. that require impact resistance [2,3]. Polymers or their blends as substitutes for currently fielded materials offer lower density, better fracture resistance and higher energy absorption under impact [4,5] conditions. One such family of polymers of interest is interpenetrating polymer networks or IPNs. These are polymer systems comprising of two or more networks which are at least partially interlaced on a molecular scale without being chemically crosslinked, and hence inseparable unless individual crosslinks are broken [6,7]. They can be synthesized using *sequential* processing, where one network is formed and infused with the second monomer reagent in two serial steps, or *simultaneous* processing, where all the constituents are allowed to react simultaneously [6,8]. Since the first detailed study on IPNs by Millar [9], a great deal of research on IPNs [10–14] has been reported in the past few decades. The resulting multicomponent material offers a promising approach for combining the best properties of different polymers synergistically. Thus, a polymer composite could be engineered with desirable characteristics such as stiffness, strength, toughness, optical transparency, etc. In the early works done by Chen et al. [15] and Fan et al. [16], vinyl ester resin (VE) was used with a polyurethane network for synthesizing IPNs via simultaneous process. Here, the formation of crosslinks between networks was never the objective, and hence the generation of crosslinks was avoided. The morphology of the IPN showed phase separation between the networks. Recently, Bird et al. [17] synthesized IPNs based on polyurethane(PU) and poly (methyl methacrylate) (PMMA). They demonstrated a high degree of transparency for certain compositions with mild phase separation, while certain other compositions showed significant phase separation. The composition with PMMA:PU of 80:20 showed higher elastic modulus, glass transition temperature and optical transparency. Jajam et al. [5] subsequently studied the mechanical characteristics of these IPNs using the optical method of Digital Image

* Corresponding author.
E-mail address: tippuhv@auburn.edu (H.V. Tippur).

https://doi.org/10.1016/j.polymertesting.2018.06.032
Received 4 April 2018; Accepted 25 June 2018
Available online 27 June 2018

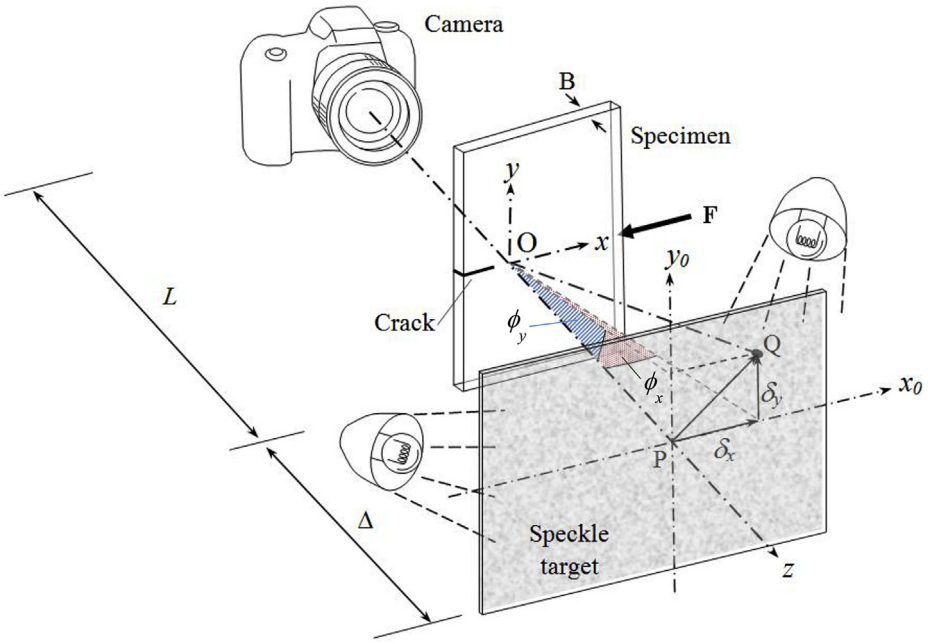

Fig. 1. The schematic of the experimental setup for transmission-mode Digital Gradient Sensing (DGS) technique to determine stress gradients in transparent sheets [25].

Correlation (DIC). They reported a reduction in the elastic modulus, loss of strength and increase in ductility with increase in PU fraction. Their 85:15 IPN formulation showed ~60% and ~40% improvement in fracture toughness over commercial PMMA under quasi-static and dynamic loading conditions, respectively.

The IPNs usually show some degree of phase separation during synthesis. This has been observed in both simultaneous and sequential polymerization approaches employed for synthesizing IPNs [18,19]. Chen et al. [20] and Lian et al. [21] synthesized a multicomponent system from a vinyl ester resin (VE) along with a polyurethane phase. This VE resin was capable of undergoing stepwise polymerization as well as free radical polymerization, generating a graft-IPN. Hsieh et al. [22,23] synthesized graft-IPNs based on PU and epoxy by simultaneous polymerization to study the effect of PU to epoxy ratio. The optimum composition with higher impact strength and fracture energy was observed to be between 80:20 and 70:30 resulting from an intimate interpenetration between PU and epoxy in the graft structure. Further, Hsieh et al. [24] synthesized graft-IPNs based on urethane-modified bismaleimide (UBMI) and epoxy. The optimum composition was determined to be 15% UBMI. Although improvement in mechanical characteristics was reported in all these studies, there has been limited insight into their dynamic/impact characteristics, and the optical transparency was relatively low. For applications such as transparent armor, the characteristics of strength, stiffness and fracture toughness, as well as optical transparency, must be optimized. With this intent, authors recently synthesized graft-IPNs using polyurethane (PU) and acrylic copolymer (CoP) [1]. PU offers good ductility and energy absorption capabilities, whereas acrylate provides stiffness and impact strength, while both render superior optical transparency.

In this work, the material processing and mechanical characterization of transparent graft-IPNs were studied, including their response to dynamic/impact loading, which is largely unreported for such polymer networks. The dynamic properties need to be understood if these transparent graft-IPNs should find application as windshield of an armored vehicle, canopy of an aircraft, bullet resistant barrier, etc. Thus, the mechanical behavior, including quasi-static and dynamic fracture, of transparent acrylic/polyurethane graft-IPNs made from poly (tetramethylene ether) glycol (PTMG) of different molecular weights (650 g mol^{-1} and 1400 g mol^{-1}) were studied. Quasi-static tension and fracture tests were carried out first followed by dynamic fracture tests using a modified Hopkinson pressure bar. The measurements during dynamic loading were made using a full-field optical technique called Digital Gradient Sensing (DGS) in conjunction with ultrahigh-speed photography. These are described in the following sections starting with a brief description of DGS. This is followed by essential details on material systems and synthesis. The details on material characterization, optical transparency, specimen geometry, and the testing approach are discussed next. Experimental results including elastic and failure responses of different compositions, quasi-static and dynamic fracture behavior etc. are presented subsequently along with relevant fractography.

1.1. Optical method: Digital Gradient Sensing (DGS)

A schematic representation of the experimental setup for transmission-mode DGS is shown in Fig. 1. In transmission-mode DGS, a random speckle pattern on a planar surface, referred to as the target, is photographed through optically transparent planar sample being studied. Ordinary white light illumination is used for recording random gray scales on the target. The speckle pattern is first photographed through the specimen in its undeformed state to obtain a reference image. That is, a point P on the target plane (x_0 - y_0 plane) is recorded by a pixel of the camera through point O on the specimen plane (x – y plane). On loading, the non-uniform state of stress changes the refractive index of the specimen in the vicinity of stress concentration (or crack-tip in this work). Additionally, the Poisson effect produces non-uniform thickness changes. A combination of these, known as the *elasto-optical effect*, causes the light rays to deviate from their original path as they

propagate through the crack-tip vicinity. The speckle pattern is once again photographed through the specimen in the deformed state. Then, a neighboring point Q on the target plane is recorded by the same pixel of the camera through point O on the specimen plane after deformation. The local deviations of light rays can be quantified by correlating speckle images in the deformed and reference states. Once displacements δ_x and δ_y are evaluated using digital image correlation algorithms to correlate the speckle images in the deformed and reference states, the angular deflections of light rays ϕ_x and ϕ_y in two orthogonal planes (x-z and y-z planes, the z-axis coinciding with the optical axis of the setup and x-y being the specimen plane coordinates) can be computed by using the known distance between the specimen plane and the target plane. A detailed analysis by Periasamy and Tippur [25] showed that the local angular deflections are related to the gradients of the in-plane normal stresses as,

$$\phi_{x;y} = \pm C_\sigma B \frac{\partial(\sigma_x + \sigma_y)}{\partial x;\, y} \tag{1}$$

where C_σ is the elasto-optic constant of the material, B is its initial thickness and σ_x and σ_y denote the thickness-wise averages of Cauchy's normal stress description. Previous reports having elaborated the applicability of this method to perform fracture studies in other commonly used transparent structural materials such as PMMA [26], polycarbonate [4] and glass [27] [28], its applicability to graft-IPNs is deemed feasible.

2. Material synthesis

The graft-IPNs were synthesized in a single-step using polyurethane and the copolymer phases whose constituents were mixed separately at room temperature. The polyurethane phase (PU) was synthesized from three different polyols: 2-ethyl-2-(hydroxymethyl)-1,3propanediol (TRIOL) from Acros Organics, (USA), and poly (tetramethylene ether) glycol (PTMG) average $M_n \sim 650$ and $\sim 1400\ g\ mol^{-1}$ from Sigma-Aldrich, (USA). A mix of TRIOL and PTMG was made beforehand through melting. The mixture was kept melted in an oven under vacuum to prevent moisture infiltration. The same procedure was repeated for different PTMGs employed in the synthesis. The isocyanate used was hexamethylene diisocyanate 98.0% (DCH) from TCI, (USA). Dibutylin dilaurate, 98% (DD) by Pfaltz & Bauer, (USA) and triphenylbismuth, 99+% (TB) from Alfa Aesar, (USA), were used as

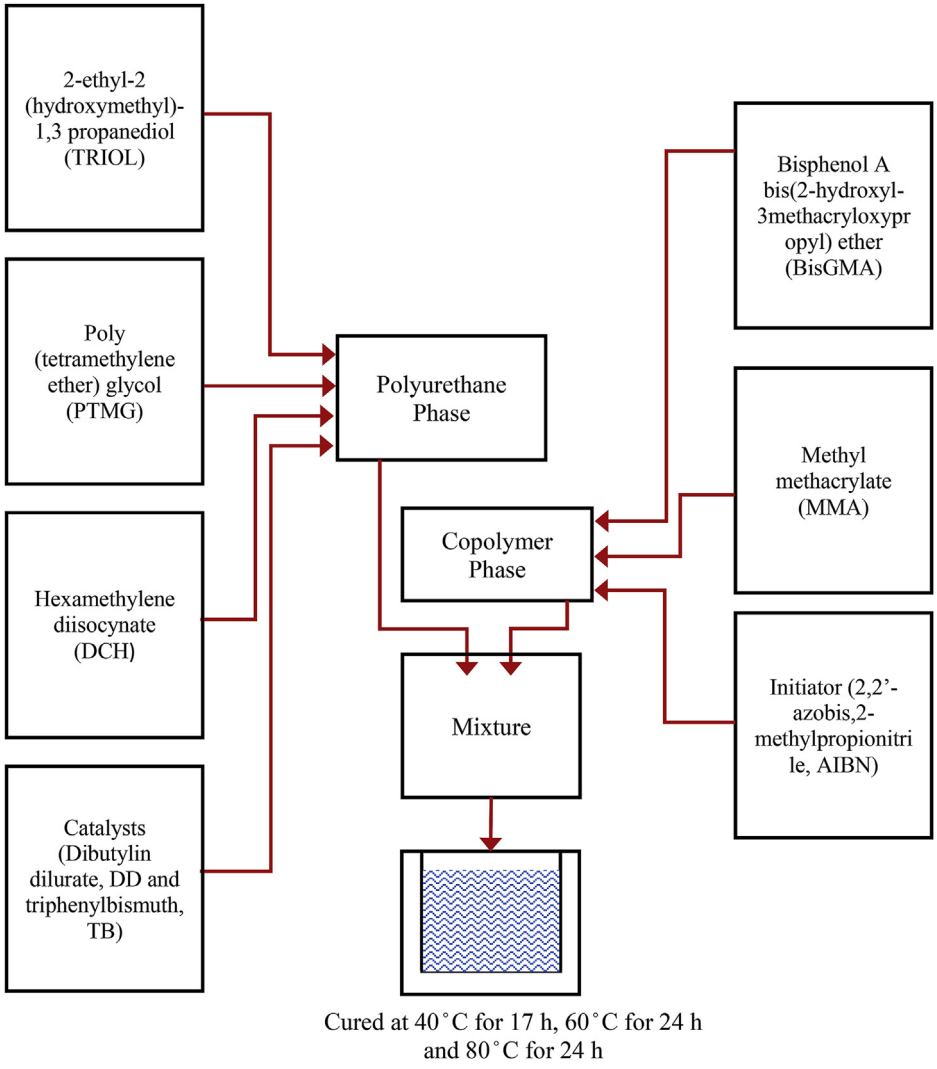

Fig. 2. Schematic of graft-IPNs synthesis steps.

Table 1
The list of all compositions of graft-IPNs synthesized.

MMA:BiSGMA ratio in CoP by wt%	Mol wt of PTMG in PU	CoP:PU ratio by wt%	Grade
90:10	650 g mol^{-1}	60:40,70:30,75:25,80:20 and 90:10	1
	1400 g mol^{-1}	60:40,70:30,75:25,80:20 and 90:10	2

catalyzers for the synthesis, while ethyl acetate was employed as an analogue for both catalyzers. The constituents of the copolymer (CoP) phase consisted of bisphenol A bis(2-hydroxy-3-methacryloxypropyl) ether (BisGMA) from Esstech, (USA) and two different acrylic monomers: methyl methacrylate (MMA) 99% stabilized from Alfa Aesar, (USA). 2,2′-azobis (2-methylpropionitrile), (AIBN) 98% from Sigma-Aldrich, (USA) was used as a thermal initiator for the reaction.

To prepare the mixture for copolymer phase (CoP), MMA and the BisGMA resin were mixed at a mass ratio of 90:10 MM A:BisGMA. Thermal initiator of mass equivalent to 1 wt% of the total copolymer mass was added for the polymerization. Next, the diisocyanate was added to the PTMG/TRIOL mixture keeping the following ratio: 0.19eq TRIOL: 0.12eq PTMG: 0.31eq DCH. An additional amount of DCH was added to generate crosslink points between networks, according to the equivalence ratio of 1:1 DCH:BisGMA. Once PU and CoP phases were prepared separately, they were mixed together and catalyzers for both the phases were added to the mixture. The resulting mixture was poured into rectangular molds prepared from glass sheets. Subsequently, all molds (containing the uncured sample) were placed in an oven at 40 °C for 17 h after which the samples were transferred to a water bath at 60 °C for 24 h and, finally, the temperature of the water bath was increased to 80 °C for another 24 h. This is schematically represented in Fig. 2.

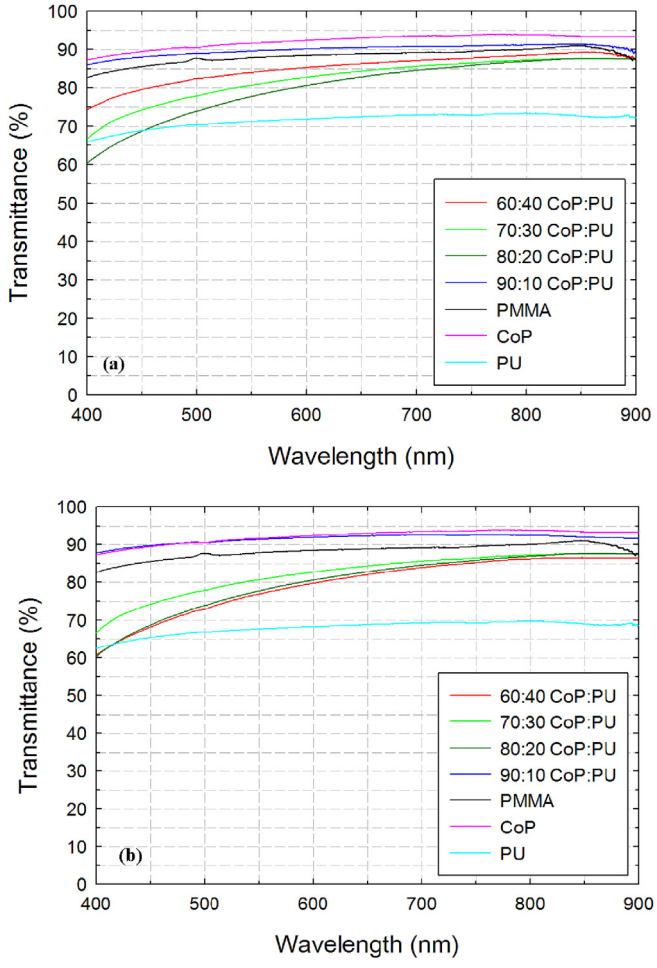

Fig. 3. Optical transmittance obtained using UV–visual spectroscopy for (a) grade-1 and (b) grade-2 graft-IPNs.

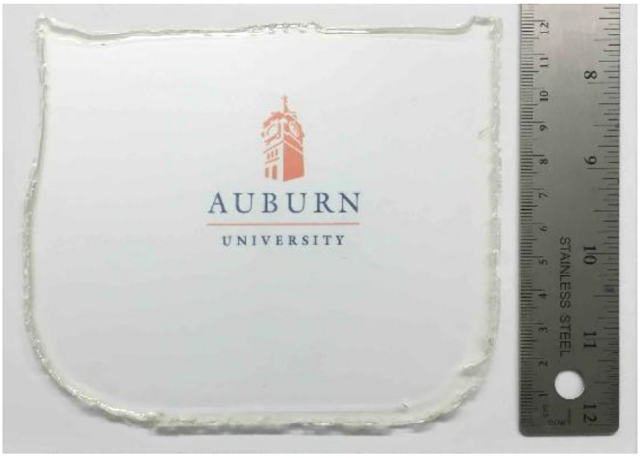

Fig. 4. A clear and sharp photograph of Auburn University logo through the cast specimen of a select (70:30 Cop:PU) grade-1 graft-IPN.

The graft-IPNs samples with different compositions were thus produced. The CoP to PU ratio was varied from 90 wt% and 10 wt%, to 60 wt% and 40 wt%. This change in the ratio was applied for two grades of graft-IPNs obtained by using 650 g mol^{-1} and 1400 g mol^{-1} of PTMG in synthesis of the PU phase. The various compositions synthesized are listed in Table 1.

2.1. Optical transparency

The graft-IPNs were examined using UV–visible spectroscopy to measure optical transmittance [1]. The transmittance of PMMA, CoP and PU were also measured and compared with that of graft-IPNs. Fig. 3(a) and (b) show plots of wavelength of light and corresponding transmittance of various compositions of grade-1 and -2 graft-IPNs, respectively. The graft-IPNs presented a relatively high degree of transparency with transmittance between 75% and 90%, quite comparable to that for PMMA, and significantly higher than the PU phase. These results also confirm a high degree of interpenetration achieved on both systems, regardless of the molecular weight of the PTMG used. Fig. 4 shows the photograph of Auburn University logo through a select composition (70:30 CoP:PU) of grade-1 graft-IPN. The logo is uniformly and clearly visible through the specimen. Also, no visible evidence of

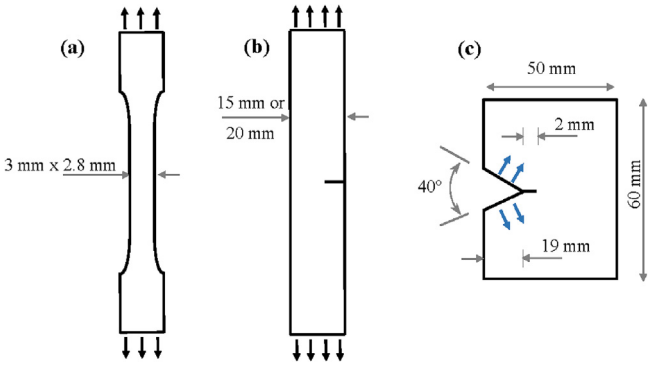

Fig. 5. The schematic showing the specimen geometry and loading configuration used for (a) quasi-static tension tests, (b) quasi-static fracture tests, and (c) dynamic fracture tests. Sample thickness were 2.8 mm and 4.8 mm for quasi-static and dynamic tests respectively. (Note: Thickness of each specimen was measured and used to evaluate the properties.)

macroscopic phase separation is observed.

2.2. Specimen fabrication and geometry

The specimen geometries used in this study are shown in Fig. 5(a)-(c). The cured graft-IPN sheets of 2.8 mm thickness were machined into dumbbell shaped specimens for performing tension tests (see Fig. 5(a)). Dimensions of the standard test methods could not be strictly adhered to because of the limited availability of processed material. For quasi-static fracture tests, the graft-IPN sheets of 2.8 mm thickness were machined into rectangular SEN samples of dimension 70 mm × 15 mm for grade-1 graft-IPNs and 70 mm × 20 mm for grade-2 graft-IPNs (see Fig. 5(b)). An edge notch was cut on the longer edge using a diamond impregnated wafer blade, and the notch tip was further sharpened by scoring the root with a steel razor blade before testing.

For dynamic fracture experiments, the specimens of slightly higher thickness (4.8 mm) were used to avoid buckling and bending during the initial compressive stress wave loading (to be discussed later). Plate specimens of dimensions 60 mm × 50 mm (see Fig. 5(c)) with a 40° V-notch machined on the longer edge that matched the impact end of a modified Hopkinson bar [29]. Using a diamond impregnated wafer blade, the notch was extended by 2 mm and sharpened using a steel razor blade, as in the static counterparts.

2.3. Quasi-static tests

2.3.1. Uniaxial tension

The uniaxial tension tests were carried out using an Instron 4665 universal testing machine (UTM) in displacement control (crosshead speed 0.015 mm/s) mode. Three specimens were tested for each composition. An extensometer (gage length 6.35 mm) was used to measure the longitudinal strain. The loading configuration is shown in Fig. 5(a).

The tensile stress-strain response of grade-1 graft-IPNs along with commercial PMMA is shown in Fig. 6(a). Initial response indicates a linear elastic region, followed by a nonlinear regime leading to an abrupt failure in the case of PMMA, whereas graft-IPNs show significant nonlinearity. Except for 90:10 compositions which failed at ~3% strain, the graft-IPNs did not fail up to 20% strain, the maximum strain capacity of the extensometer used during these experiments. For 90:10 graft-IPNs the failure occurred at ~62 MPa, whereas 80:20, 70:30, 75:25 and 60:40 showed an ultimate stress of ~60 MPa, ~52 MPa, ~37 MPa and ~18 MPa, respectively. Thus, there was substantial decrease in the ultimate stress as the PU content is increased. The elastic modulus for each composition was determined from the slope of the stress-strain curve at < 0.2% strain and are shown in Fig. 6(b). Each data point represents an average value based on multiple specimens (typically three, due to limited availability of material) and the error bars corresponds to the bounds of the data spread. As expected, there is clear evidence of decrease in the elastic modulus with increase in the PU content. Further, these graft-IPNs continued to remain transparent until the extensometer limit of 20% strain, as shown in the inset of Fig. 6(b). Similar tensile (stress-strain) responses were observed for grade-2 graft-IPNs and are shown in Fig. 7(a). Except for the 90:10 composition for which failure was at ~11% strain, the graft-IPNs did

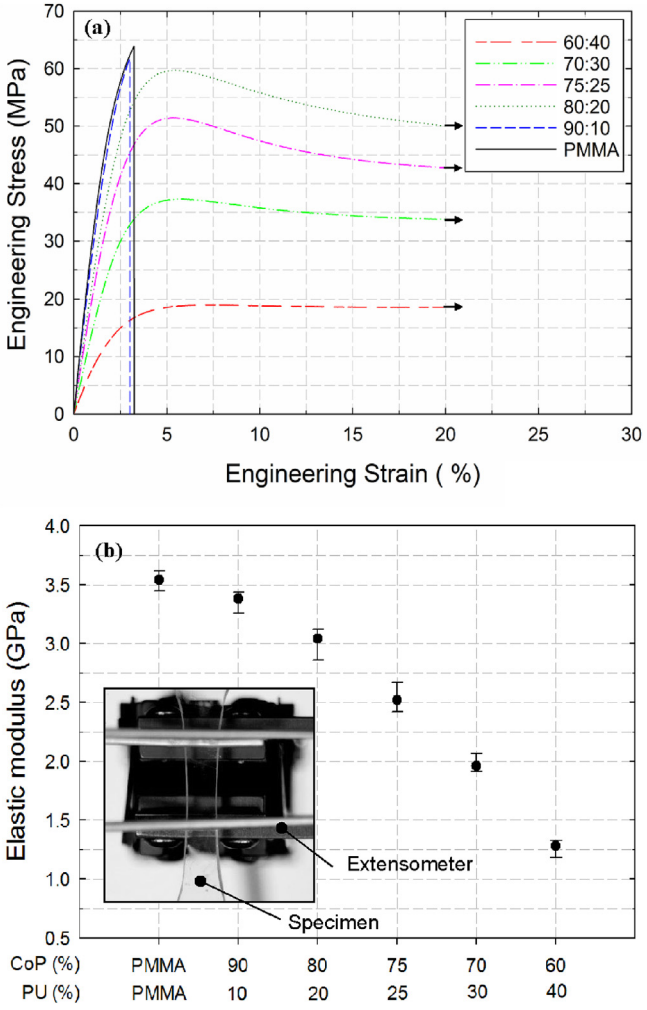

Fig. 6. (a) Stress vs. strain response from tension tests, and (b) compilation of the elastic moduli for grade-1 graft-IPNs. Also included are data for commercial PMMA. Inset shows the photograph of 75:25 grade-1 graft-IPN at 20% strain, wherein the specimen remains transparent. (Note: The arrow at the end of the plot shows that the specimen did not fail at the extensometer strain limit of 20%. Error bar represents the bounds of the data spread).

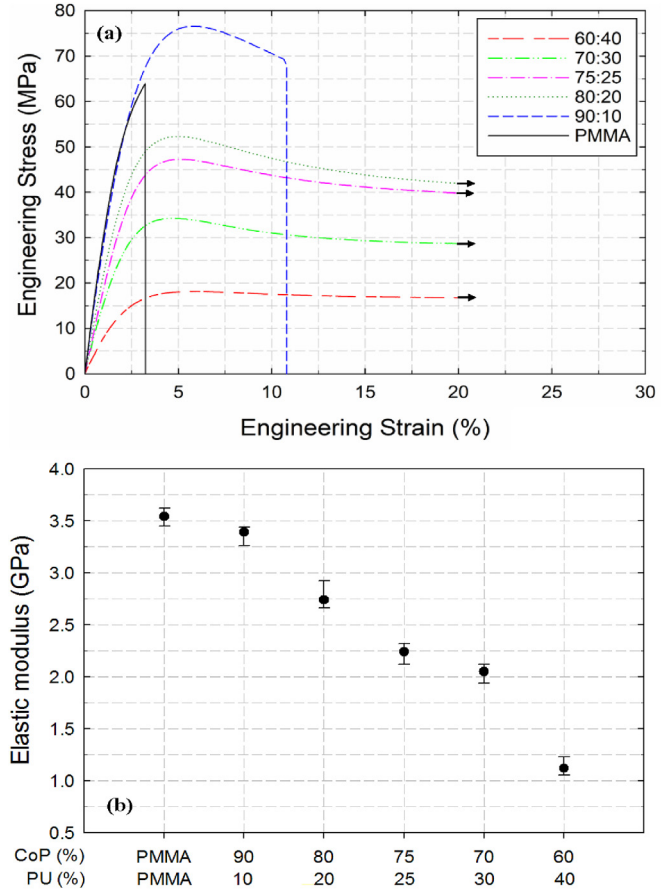

Fig. 7. (a) Stress vs. strain response from tension tests, and (b) compilation of the elastic modulus for grade-2 graft-IPNs. Also included are data for commercially procured PMMA. (Note the arrow at the end of the plot shows that the specimen did not fail at the extensometer strain limit of 20%%. Error bar represents the bounds of the data spread).

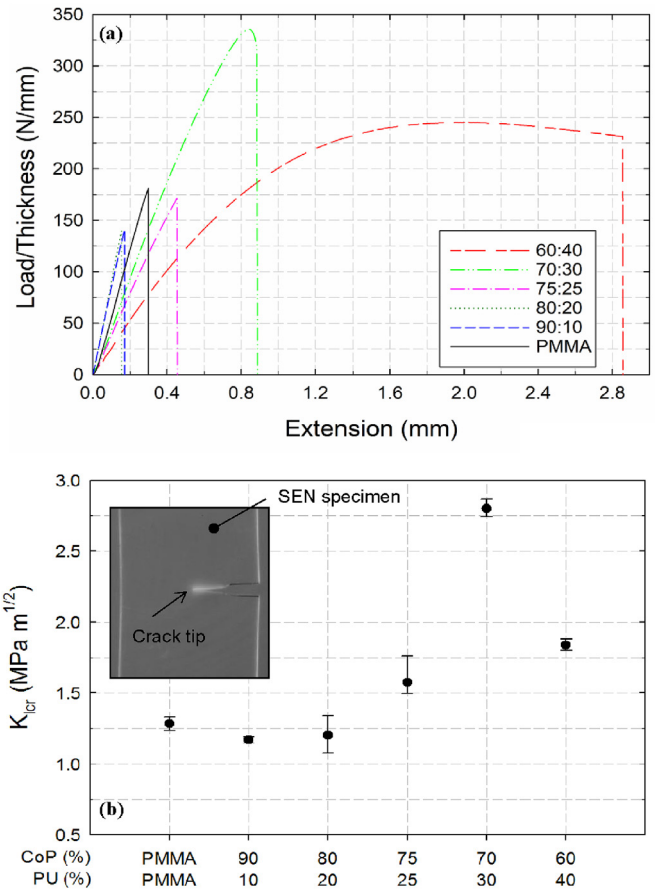

Fig. 8. Quasi-static fracture results for grade-1 graft-IPN: (a) Plot of load/thickness vs. extension obtained from fracture tests, and (b) compilation of the K_{Icr} for different compositions compared to commercial PMMA. Inset shows the photograph of 70:30 grade-1 graft-IPNs during fracture process, wherein whitening/crazing near the crack-tip can be seen. (Note: %. Error bar represents the bounds of the data spread).

not fail up to 20% strain. The graft-IPNs 90:10, 80:20, 70:30, 75:25 and 60:40 composition had ultimate stress of ~76 MPa, ~53 MPa, ~47 MPa, ~35 MPa and ~18 MPa, respectively. Similar to grade-1 graft-IPNs, there was a substantial decrease in the ultimate stress as the PU content is increased.

The elastic modulus for each composition was determined from the slope of the stress-strain curve at < 0.2% strain, as shown in Fig. 7(b). Again, each data point represents the average value from multiple specimens (three) and the error bars correspond to the bounds of the data spread. Similar to grade-1 graft-IPNs, there is a decrease in the elastic modulus with an increase in the PU content. This trend is similar to those reported by other investigators [5] [17] and is attributed to the lower elastic modulus of the PU phase. Further, in the case of grade-2 graft-IPNs, the elastic modulus for each composition was higher than the grade-1 counterparts. Similar differences between grade-1 and -2 graft-IPNs were also observed for the ultimate stress and failure strain. Hence, the increase in molecular weight of PTMG used to synthesize graft-IPNs was favorable in terms of elastic modulus.

2.3.2. Fracture tests

Quasi-static fracture tests were performed under uniaxial tensile loading conditions. The loading configuration is shown in Fig. 5(b). The SEN samples were loaded in displacement control (crosshead speed 0.015 mm/s) mode using Instron 4665 UTM. The load vs. load-point deflection data were recorded up to crack initiation and during stable crack growth phase that occurred in a few of the compositions tested. The critical mode-I stress intensity factors (SIF) at crack initiation, K_{Icr}, were calculated from the measured peak load at crack initiation as [30],

$$K_{Icr} = \frac{F_{cr}\sqrt{\pi a}}{Bw} f\left(\frac{a}{w}\right) \tag{2}$$

where $f\left(\frac{a}{w}\right) = \left[1.12 - 0.23\left(\frac{a}{w}\right) + 10.6\left(\frac{a}{w}\right)^2 - 21.7\left(\frac{a}{w}\right)^3 + 30.4\left(\frac{a}{w}\right)^4\right]$, F_{cr} is the peak load, B is the specimen thickness, a is the initial crack length and w is the width of the specimen. The a/w ratio for all samples were maintained at 0.2. Four specimens were tested for each composition based on the availability of the material.

Quasi-static fracture tests on graft-IPNs along with commercial PMMA were performed. The normalized (with respect to the specimen thickness due to slight difference in cast material) load-deflection curves for grade-1 graft-IPNs and commercial PMMA are shown in Fig. 8(a). Commercially procured PMMA showed a linear response up to the peak load, followed by a sudden drop signaling crack initiation and brittle failure. The graft-IPNs, except for 70:30 and 60:40 compositions, showed a similar response. The 70:30 composition showed as linear response for most part until the very end where a modest nonlinearity

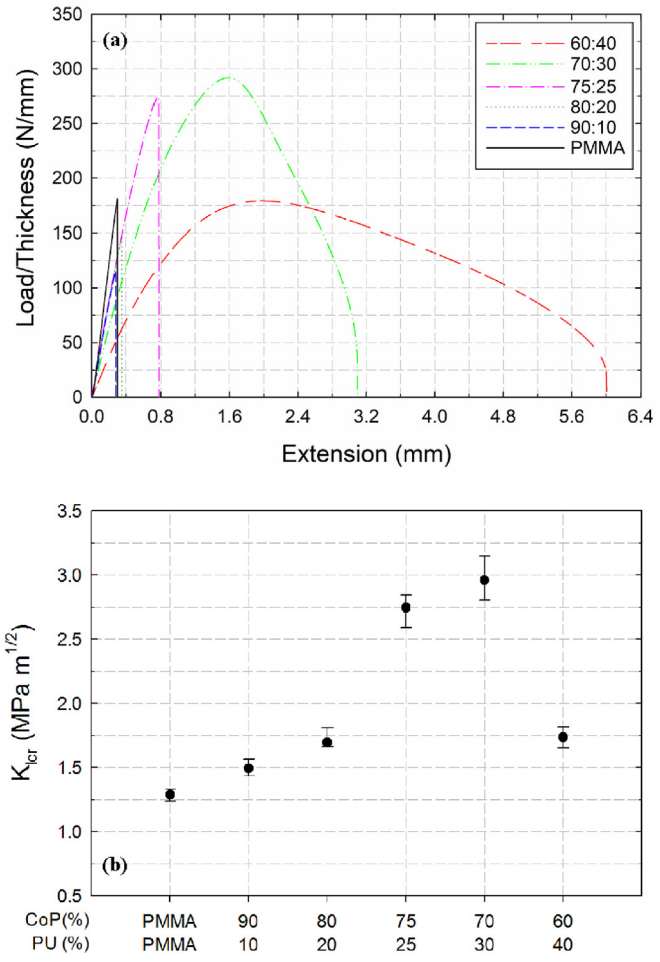

Fig. 9. Fracture test results for grade-2 graft-IPNs relative to commercially procured PMMA: (a) plot of load per unit thickness and extension (b) compilation of the K_{Icr} compared with commercial PMMA counterpart. (Note: Error bar represents the upper and lower bounds of the data spread).

can be seen before reaching the peak load, and subsequently failure. As for the 60:40 composition, the initial response was linear but it quickly changed to a nonlinear response for a while before attaining a peak load, followed by a stable crack growth where a continuous decrease in load until complete failure could be seen. The extent of nonlinearity increased with the PU content. This nonlinearity in the pre-peak load region can be attributed to crack-tip blunting and crazing prior to crack initiation. This ductility in material response was accompanied by whitening/crazing near the crack-tip, as shown in the inset of Fig. 8(b). Moreover, propagation of the macro-crack required increase of the applied load. Further, the crack exhibited a tendency to modestly deviate from its original path of propogation. The highest peak load was observed for the 70:30 composition and the largest area under the load-deflection curve representing the overall strain energy absorbed was for 60:40 compositions. The quasi-static crack initiation toughness, K_{Icr}, was calculated using the load at crack initiation in each case. The variation of K_{Icr} with CoP:PU ratio along with that of commercial PMMA is shown in Fig. 8(b). Again, each data point corresponds to an average of multiple (four) measured values of K_{Icr}. The trends in K_{Icr} values with increasing PU suggest that there is an optimum CoP:PU ratio for which the quasi-static fracture toughness is the highest. Based on these results, the 70:30 graft-IPNs showed the maximum improvement of ~115% in K_{Icr} (2.8 MPa√m) over commercial PMMA (~1.3 MPa √m).

The normalized load-deflection curve (load normalized by the sample thickness) and compiled K_{Icr} for grade-2 graft-IPNs along with the one for commercial PMMA are shown in Fig. 9(a) and (b), respectively. Similar trends as in grade-1 graft-IPNs are seen, with the optimum composition being 70:30 CoP:PU with K_{Icr} of ~3.0 MPa √m. When compared to grade-1 graft-IPNs, grade-2 graft-IPNs show an improvement in the fracture toughness (critical stress intensity factor) for each composition. Comparing the optimum composition of 70:30 CoP:PU of grade-1 graft-IPN with that of grade-2 graft-IPN, the latter showed approx. 6% improvement in K_{Icr} over the former.

2.4. Dynamic fracture tests

The dynamic fracture of graft-IPNs was studied using transmission-mode DGS in conjunction with ultrahigh-speed digital photography. A schematic representation of the experimental setup employed is shown in Fig. 10. A modified Hopkinson pressure bar (long-bar) was used for loading the pre-notched specimen. This was a 1.83 m AL 7075-T6 long-bar of 25.4 mm diameter with a wedge shaped tip (see, Fig. 10 inset) pushed against the V-notch cut into the unconstrained specimen (see Fig. 5(c) for loading configuration). A 305 mm long, 25.4 mm diameter rod held inside the barrel of a gas-gun was co-axially aligned with the long-bar and was used as the striker. Both the long-bar and the striker were made of AL 7075-T6, eliminating acoustic impedance mismatch between them during impact loading.

The speckle images were acquired using a Cordin-550 ultrahigh-speed digital camera at a resolution of 1000 × 1000 pixels on 32 independent CCD sensors positioned radially around a five-facet rotating mirror. The imaging system also included two high-energy flash lamps producing broad-band white light illumination. Experimental parameters such as the trigger delay, flash duration, framing rate, CCD gain, and data storage were controlled using a computer connected to the camera. A 28–300 mm focal length macro zoom lens along with an adjustable bellows was used for imaging the dynamic event. Further, the camera lens aperture was kept open as wide as possible (numerical aperture F$^{\#}$5.6) to achieve good exposure with minimum electronic gain setting during recording. The specimen was located approximately 850 mm in front of the camera. (Each speckle covered approximately 3–4 pixels; or a scale factor of 28–30 pixels/mm was used.) The specimen was placed on an adjustable platform with a 2 mm thick strip of soft putty pressed on the top and bottom edges of the specimen, as shown in Fig. 5. The putty strips helped achieve approximately symmetric and 'free surface' boundary conditions at the top and bottom edges. A target plate decorated with random black and white speckles was placed behind the specimen at a distance Δ = 27.4 mm away from the mid-plane of the specimen. A pair of heavy dots (Fig. 6) was marked on the target plate to help relate the dimensions on the image to the actual specimen/target dimensions.

The region-of-interest in this study was near the initial crack-tip. Accordingly, the camera was focused on a 35 mm × 35 mm square region around it. Prior to loading, a set of 32 images of the speckles were recorded through the specimen in the undeformed state at 200,000 frames per second. Sufficient care was exercised to achieve an approximately Gaussian distribution of gray scales for each image, typically in the mid-range of 0–255 (8 bit) gray scale by adjusting the flash lamps. Next, without altering any of the camera settings, the striker was launched towards the long-bar using the gas-gun at a velocity of

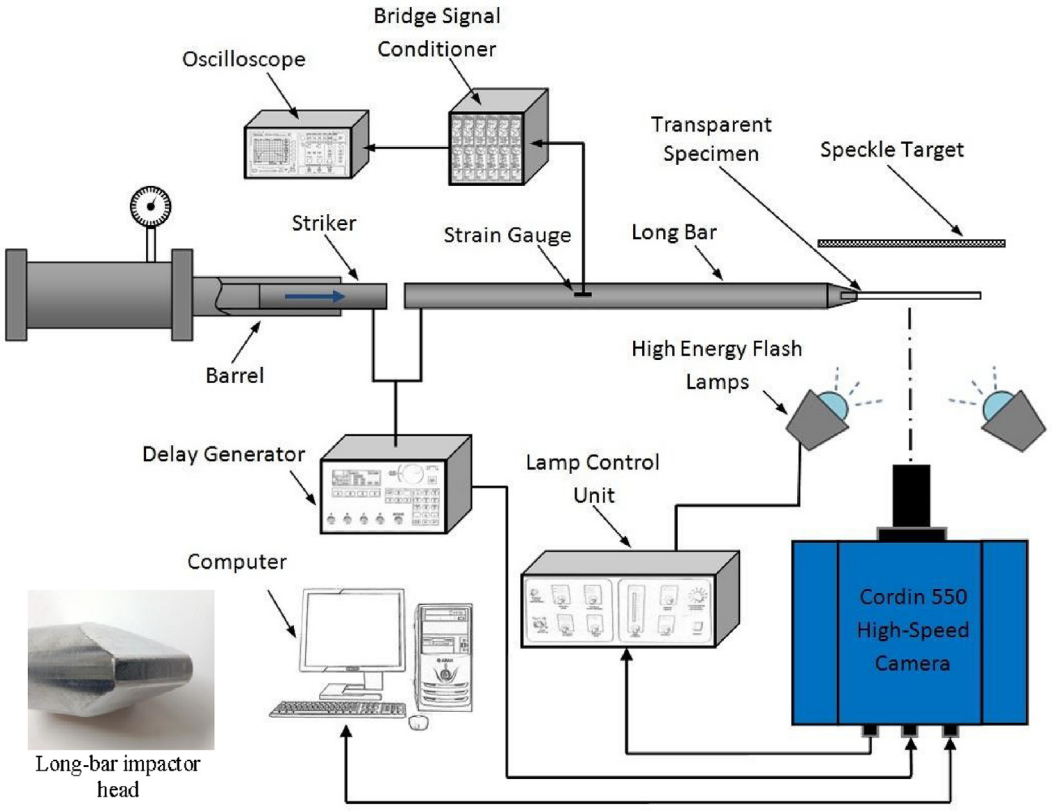

Fig. 10. Experiment setup used for conducting dynamic fracture tests on graft-IPNs using transmission-mode DGS [30].

~13.5 m/s. When the striker contacted the long-bar, a compressive stress wave was set off in the long-bar, which propagated along its length before loading the specimen. The duration of the loading phase of pulse generated was ~120 μs. When the striker contacted the long-bar, a trigger signal was also produced, which initiated the camera to record a second set of 32 images in the deformed state at the same framing rate. With a preset trigger delay, camera recorded 32 images in the deformed state. Thus, a total of 32 pairs of images in the deformed and undeformed (reference) states were recorded at 5 μs intervals between successive images. The corresponding images for each sensor were paired from the undeformed and deformed sets and each of these 32 matched pairs was correlated separately. The 2D image correlation was carried out using the image analysis software ARAMIS®. For analysis, each image was segmented into facets/sub-images consisting of 25 × 25 pixels. An overlap of 20 pixels (i.e., step size of 5 pixels) was used during image correlation. This resulted in data points in the region-of-interest for each of the two orthogonal displacement fields. The corresponding angular deflections of light rays were subsequently determined using the known distance Δ between the specimen and the target planes.

2.4.1. Evaluation of crack velocity and stress intensity factor (SIF)

The position of the crack-tip in each digitized image was used to measure the instantaneous crack length. Subsequently, the crack velocity (V) was estimated from the crack length history using backward difference method [31],

$$V_i = \frac{a_i - a_{i-1}}{t_i - t_{i-1}} \tag{3}$$

Where a and t are crack length and time, respectively, at a given instant i. The SIFs were evaluated from an over-deterministic least-squares analysis of the crack-tip data in conjunction with the asymptotic equation (see Ref. [31] for details) with $N = 4$. In the case of a propagating crack-tip the following crack-tip field,

$$\phi_x(t) = C_\sigma B \left[\begin{array}{l} -\frac{1}{2} r^{-\frac{3}{2}} \left\{ \begin{array}{l} f(V; C_L; C_S) A_1(t) cos\left(\frac{3\theta}{2}\right) \\ +g(V; C_L; C_S) D_1(t) \sin\left(-\frac{3\theta}{2}\right) \end{array} \right\} \\ + \sum_{N=2}^{\infty} \left\{ \begin{array}{l} A_N(t)\left(\frac{N}{2} - 1\right) r^{\left(\frac{N}{2}-2\right)} cos\left(\left(\frac{N}{2} - 2\right)\theta\right) \\ +D_N(t)\left(\frac{N}{2} - 1\right) r^{\left(\frac{N}{2}-2\right)} \sin\left(\left(\frac{N}{2} - 2\right)\theta\right) \end{array} \right\} \end{array} \right] \tag{4}$$

was used. In the above, f and g are functions of instantaneous crack velocity, V, (r, θ) denote the contracted crack-tip polar coordinates. Further, (r, θ) can be expressed in the local Cartesian coordinates moving with the crack-tip (x, y) as, $r = \{(x)^2 + \alpha_L^2 (y)^2\}^{1/2}$ and $\theta = \tan^{-1}\left(\frac{\alpha_L y}{x}\right)$. The coefficients of $A_1(t)$ and $D_1(t)$ in the asymptotic series are related to the mode-I and mode-II stress intensity factors $K_I(t)$ and $K_{II}(t)$, respectively, as $A_1(t) = K_I(t)\sqrt{2/\pi}$ and $D_1(t) = K_{II}(t)\sqrt{2/\pi}$. The functions f and g are,

$$f(V; C_L, C_S) = \left(\frac{1+\nu}{1-\nu}\right) \frac{(1+\alpha_S^2)(1-\alpha_L^2)}{4\alpha_L\alpha_S - (1+\alpha_S^2)^2} \; and \; g(V; C_L, C_S) = \left(\frac{1+\nu}{1-\nu}\right) \frac{2\alpha_S(1-\alpha_L^2)}{4\alpha_L\alpha_S - (1+\alpha_S^2)^2} \tag{5}$$

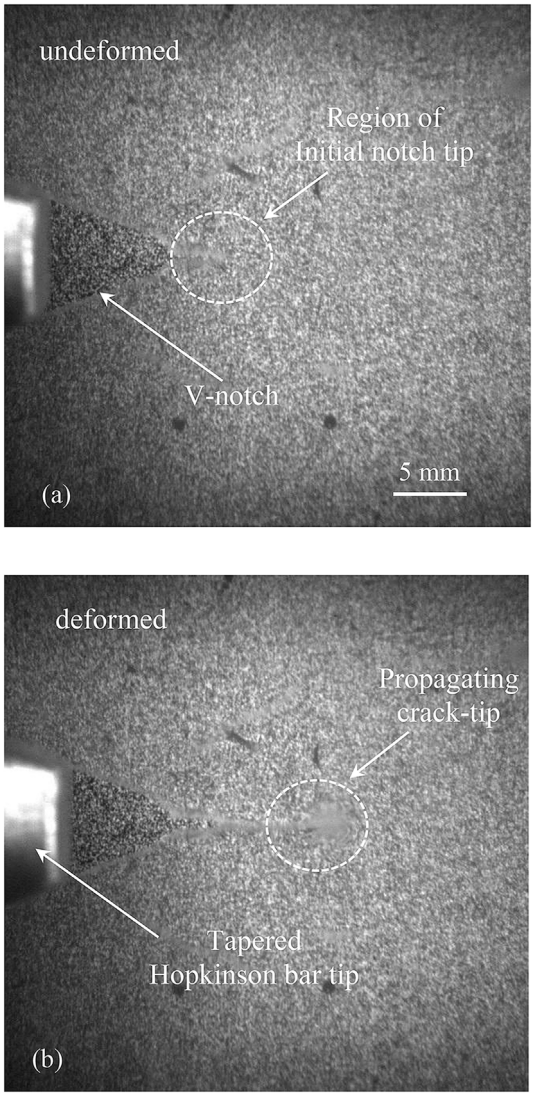

Fig. 11. Speckle images in the undeformed (top) and deformed (bottom) states recorded by the high-speed camera though a select graft-IPN specimen (80:20 CoP:PU grade-1).

where $\alpha_L = \left[1 - \frac{\rho(1-\nu)}{2\mu}V^2\right]^{\frac{1}{2}}$ and $\alpha_S = \left[1 - \frac{\rho}{\mu}V^2\right]^{\frac{1}{2}}$ for plane stress, with μ and ρ being shear modulus and mass density, respectively. Data in the region $0.35 \leq r/B \leq 0.85$ along with angular extent of $-135^\circ \leq \theta \leq 135^\circ$ near the crack-tip was used for analysis. Note that Eqs. (4) and (5) can be reduced to the form of a dynamically loaded stationary crack in the limit of the crack velocity $V \rightarrow 0$.

2.4.2. Speckle images and optical measurement of angular deflections

The recorded images, one in the undeformed and another in the deformed state for a select composition (80:20 CoP:PU) of grade-1 graft-IPN are shown in Fig. 11(a) and (b), respectively. In the deformed image, the distortion of speckles can be clearly seen near the propagating crack-tip. Fig. 12 shows the angular deflection contours, proportional to gradients in the *x*- and *y*-directions, measured using DGS at three different time instants. A clear increase in the size of contours can be seen with the passage of time, which in turn suggests an increase in SIF.

2.4.3. Crack velocity histories

Fig. 13(a) shows the crack velocity histories for grade-1 graft-IPNs along with commercial PMMA. Here, $t = 0$ denotes crack initiation at the original notch tip. After initiation, the crack accelerated to attain a maximum velocity, followed by a nearly steady but oscillatory velocity. As the PU content increased to 10%, the steady state velocity increased, although comparable to that for commercial PMMA. Subsequently, the steady state velocity dropped sharply for the 20% PU case and later increased until PU content was 40% (the maximum PU content studied). The steady state crack velocity for PMMA specimens was ~320 m/s, whereas graft-IPNs show a velocity between 120 and 450 m/s with 80:20 composition having the lowest and 60:40 the highest. This suggests a potential change in micromechanism when the CoP:PU ratio reached 80:20. This variation is shown as a function of CoP:PU ratio in Fig. 13(b). Similar trends in velocity histories were also seen for grade-2 graft-IPNs. The variation of its steady state crack velocity is shown in Fig. 14. Again, the steady state velocity for these compositions varied between 180 and 430 m/s, with 80:20 composition having the lowest and 60:40 the highest.

2.4.4. Stress intensity factor (SIF) histories

The measured stress intensity factor histories for grade-1 graft-IPNs are shown in Fig. 15(a). Time $t = 0$ represents the instant of crack initiation at the original notch tip. During the pre-initiation period, there is a monotonic somewhat linear increase in K_I until it reaches a critical value at which the crack initiated. This behavior is typical for all graft-IPN compositions. Further, there is a reduction in the overall SIF as the PU content is increased to 10%, after which there is an increase at 20% PU, and later it again decreased until the PU content reached 40%. This correlates well with the observed steady crack velocity histories (Fig. 13). That is, the crack velocity decreased correspondingly with increase in the critical SIF values (resistance to fracture) showing a higher resistance to crack initiation and possibly growth. Note that the 80:20 composition showed delayed crack initiation compared to other compositions (say, 60:40), described by the longer loading curve in the pre-initiation period, indicating that the crack initiation can be altered by changing the CoP:PU ratio. This can be attributed to lower wave speeds with increased PU content and higher ductility. The SIF at crack initiation for various compositions are shown in Fig. 15(b). When compared with PMMA (1.08 MPa√m), the optimum composition of 80:20 (3.12 MPa√m) shows ~180% improvement in K_{Icr}. These trends can be observed in both pre-initiation and post-initiation regimes. When compared with the K_{Icr} for polycarbonate, Lexan-9034, reported by Sundaram and Tippur [4] under similar dynamic loading conditions (2.25 MPa √m), the 80:20 composition showed ~38% improvement and 75:25 showed a similar result (2.08 MPa √m). Hence, some compositions of graft-IPNs have a fracture response similar to, if not better than, those for commercial polycarbonate. The SIF histories of grade-2 graft-IPNs show a similar trend as that of grade-1 graft-IPNs. Fig. 16 show the K_{Icr} for grade-2 graft-IPNs. Unlike the quasi-static results, the grade-1 graft-IPN performed better than grade-2 graft-IPN under dynamic loading.

2.4.5. Fracture surface morphology

The fracture surfaces of grade-1 samples from the dynamic fracture tests were inspected using an optical microscope at 20X magnification, and the micrographs obtained are shown in Fig. 17(a)-(f). In Fig. 17(a), PMMA sample shows no significant features apart from occasional conic marks typical of brittle fracture in glassy polymers. Each conic mark has an “eye’ or a ‘nucleus’ from where linear fracture trail emanates. In case of 90:10 graft-IPN (Fig. 17(b)) these features have become

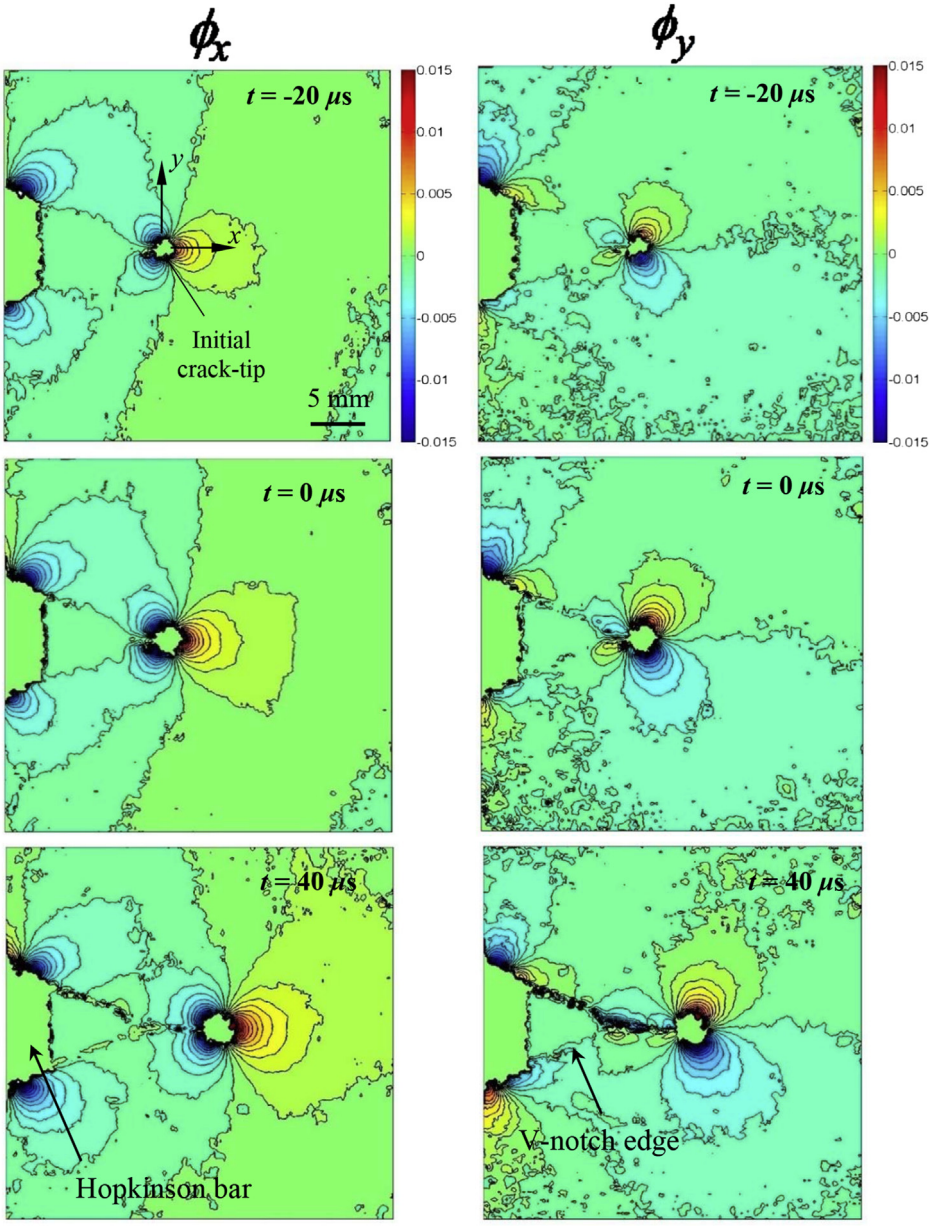

Fig. 12. Angular deflection contour plots (contour interval = 1×10^{-3} rad) proportional to stress gradients of $(\sigma_x + \sigma_y)$ in the *x*- and *y*-directions for a select graft-IPN specimen (CoP:PU 80:20 grade-1). (Note that $t = 0$ in these correspond to the time instant at crack initiation at the original notch tip.)

smaller but increased in number. This trend continues with 80:20 (Fig. 17(c)) case showing quite prominent and numerous surface features, which suggests a substantial increase in surface roughness during crack growth. Further increase in PU% increases the size of these conical features (Fig. 17(d)-(e)) but reduces their prominence as well as their frequency. Further increase in the PU% (Fig. 17(f) results in a change in the shape, from parabolic to narrow aerofoil-like features. These transitions of surface features in the micrographs seem to qualitatively explain the changes in the magnitude of the measured critical values of SIFs.

3. Conclusions

The processing and mechanical behavior under both quasi-static and dynamic loading of various *transparent* graft-IPN compositions made of soft polyurethane (PU) and stiff acrylate copolymers (CoP) were studied. The CoP to PU ratio was varied from 90 wt% and 10 wt% to 60 wt% and 40 wt%. This change in the ratio was applied for two grades of graft-IPNs obtained using 650 g mol^{-1} and 1400 g mol^{-1} of PTMG to synthesize the PU phase. Uniaxial tension tests on dumbbell shaped samples were conducted to evaluate the quasi-static stress-strain behavior and obtain elastic moduli and ultimate stress values. Tests on single edge notched (SEN) tension specimens yielded the crack initiation and growth characteristics under quasi-static conditions. The

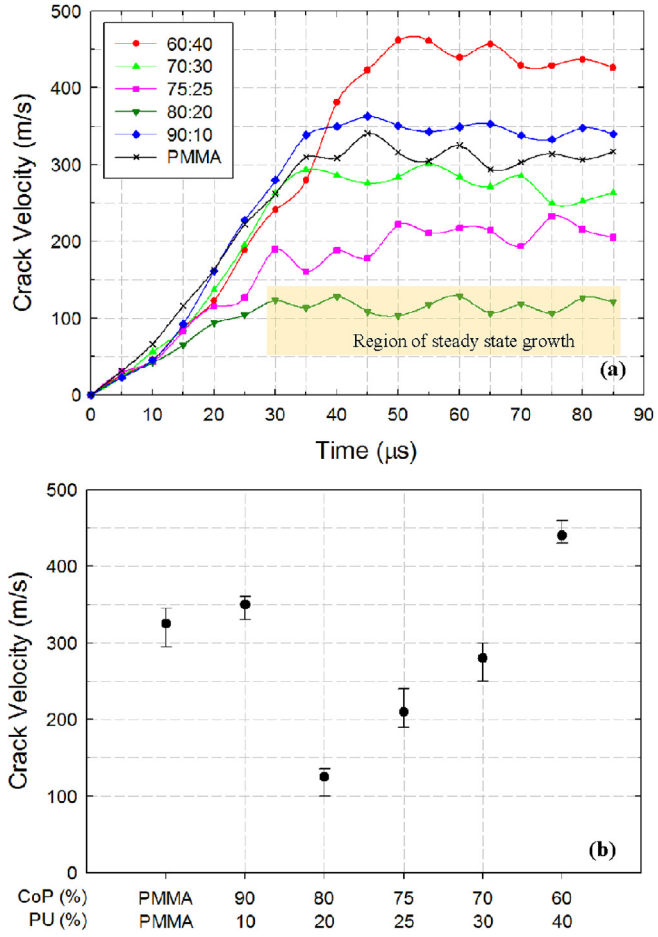

Fig. 13. Crack growth behavior of grade-1 graft-IPNs: (a) crack velocity histories and (b) steady state crack velocity variation (t = 0 corresponds to crack initiation at the original notch tip. (Note: Steady state crack velocity was obtained by averaging the velocities in the highlighted region. Error bar represents the bounds of the data spread).

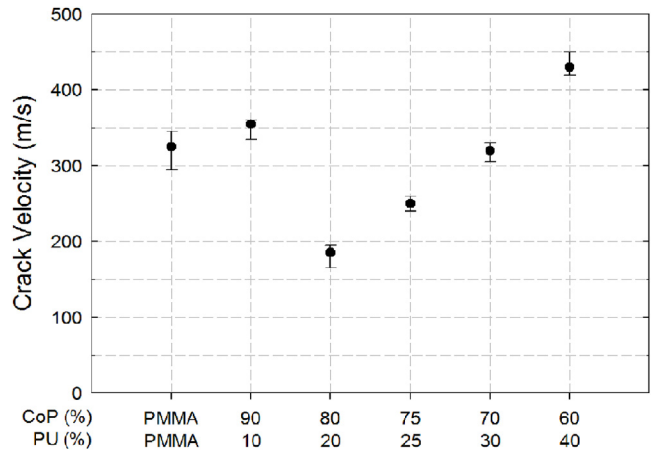

Fig. 14. Variation of steady state crack velocity for grade-2 graft-IPNs. (Note: Error bar represents the bounds of the data spread).

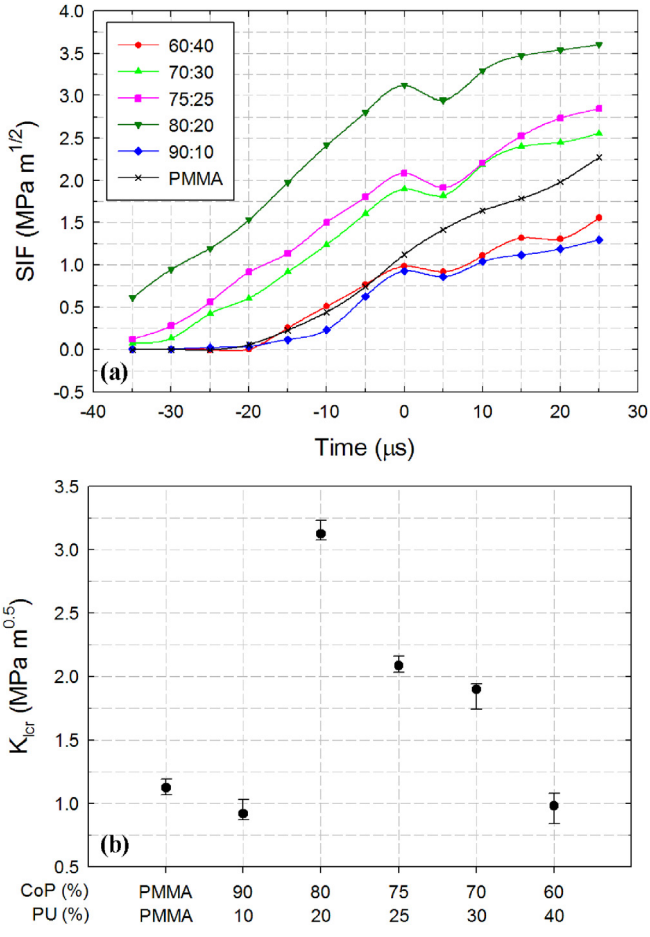

Fig. 15. Stress intensity factor (SIF) histories (top) and critical value of mode-I SIF at initiation (bottom) for grade-1 g-IPNs (t = 0 corresponds to crack initiation. Error bar represents the bounds of the data spread obtained from multiple experiments).

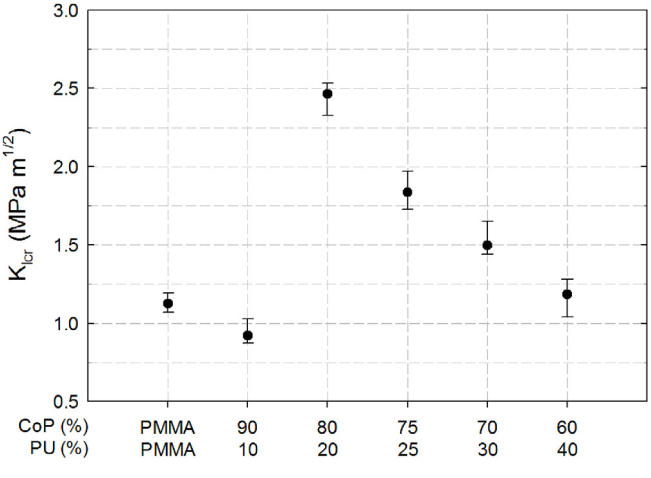

Fig. 16. Variation of dynamic K_{Icr} for grade-2 graft-IPNs. (Error bar represents the bounds of the data spread).

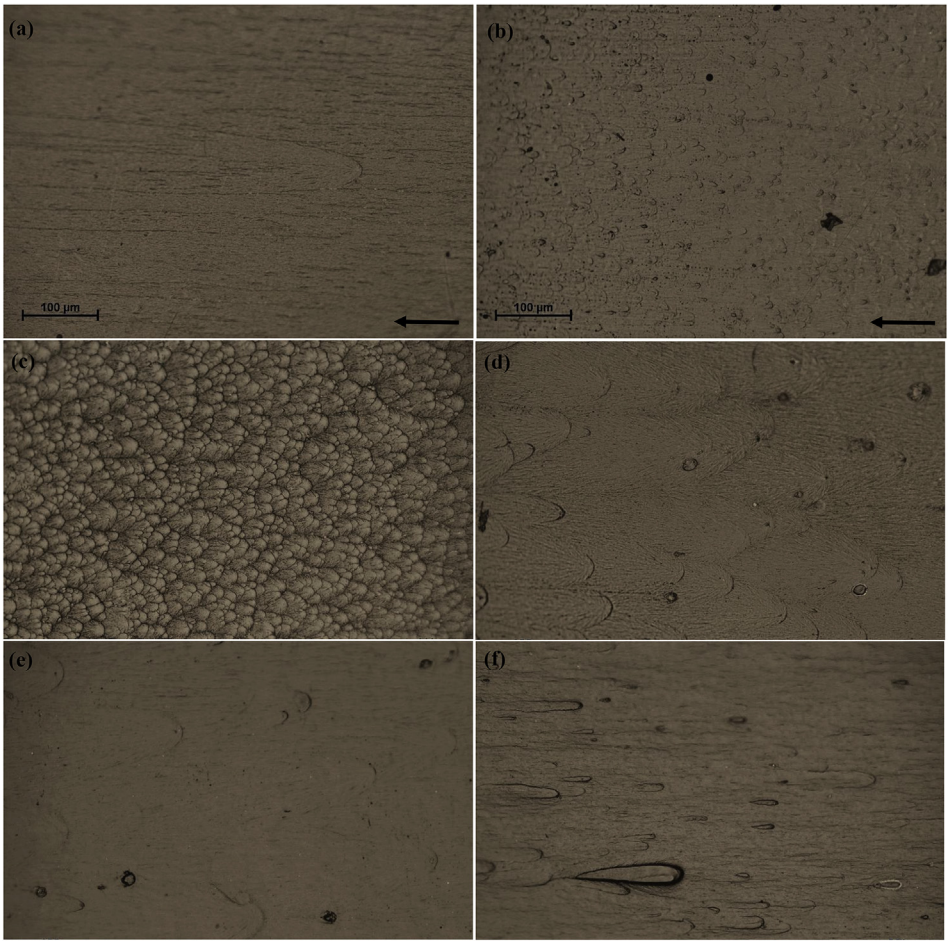

Fig. 17. Micrographs of grade-1 graft-IPNs with CoP:PU ratios of (a) PMMA, (b) 90:10, (c) 80:20, (d) 75:25, (e) 70:30 and (f) 60:40. Arrow shows crack growth direction. Scale and the arrow shown in (a) and (b) are applicable for all the figures.

dynamic fracture characteristics namely, the crack velocity and stress intensity factor history, for all the compositions were evaluated under dynamic loading conditions optically using a full-field non-contact measurement technique called DGS in conjunction with ultrahigh-speed photography. The major observations of this study are:

- All the compositions of graft-IPNs showed excellent optical transparency. Furthermore, they continued to be transparent up to 20% tensile strain.
- Elastic moduli of graft-IPNs gradually decreased by 60–70% with increase in PU phase in both grades of graft-IPNs.
- Quasi-static tensile tests showed a transition from brittle to ductile behavior when the PU phase exceeded 10% for grade-1 and 20% for grade-2 graft-IPNs.
- Quasi-static fracture tests indicate brittle unstable crack growth for 90:10, 80:20, and 75:25, grade-1 graft-IPN compositions which transitioned to brittle stable crack growth for 70:30, and finally to ductile crack growth for 60:40. This ductile behavior was accompanied by crazing near the crack-tip during crack initiation and subsequent propagation. Similar behavior was seen for grade-2 graft-IPNs except for ductile crack growth behavior for 70:30 composition.
- Maximum quasi-static fracture toughness was obtained for 70:30 graft-IPNs in both the grades ($\sim$2.8 MPa$\sqrt{m}$ and $\sim$2.95 MPa$\sqrt{m}$, respectively) with grade-2 slightly outperforming grade-1. When compared to PMMA, graft-IPNs showed an improvement of 115–120%.
- Dynamic fracture tests showed significantly lower crack speeds or higher crack growth resistance for 80:20, 75:25, and 70:30 graft-IPNs of both grades compared to PMMA, while 60:40 and 90:10 showed a higher crack speed.
- Dynamic fracture tests further indicate an improvement in crack initiation toughness over PMMA for 80:20, 75:25, and 70:30 graft-IPNs with peak value being $\sim$3.1 MPa$\sqrt{m}$, and $\sim$2.5 MPa$\sqrt{m}$ for 80:20 graft-IPN of grades-1 and -2, respectively. This is an improvement of approx. 180% and 120% over PMMA. When compared to commercially available polycarbonate, this represents an improvement of approx. 10% and 35%, respectively. However, 60:40 and 90:10 graft-IPNs of both grades of graft-IPNs showed a reduction in crack initiation toughness.

Acknowledgement

The support of the U.S. Army Research Office through grant W911NF-12-1-0317 is gratefully acknowledged.

Appendix-A

Evaluation of elasto-optic constant for graft-IPNs

The elasto-optic constant of graft-IPNs was evaluated by performing edge loading experiments on a sheet of the specimen, also referred to as the Flamant problem [4]. That is, a line-load was applied on an edge of a large planar sheet and optical measurements were made. A rectangular sheet of 50 mm × 60 mm and thickness 4.8 mm was placed on a flat rigid platform and subjected to a line-load, as shown in Fig. A1. An Instron 4465 UTM was used for loading the specimen in a displacement control mode (crosshead speed of 0.005 mm/s). A target plate coated with random black and white speckles was placed behind the specimen at 27.4 mm from the mid-plane of the specimen. A Nikon D100 digital SLR camera fitted with a 70–300 mm focal length lens and extension tube was used to record the speckles. The camera was placed in front of the specimen at a distance (L) of ~600 mm with the camera focused on a uniformly illuminated target plane through the specimen. A camera resolution of 1504 × 1000 pixels was used to acquire 8 bit images.

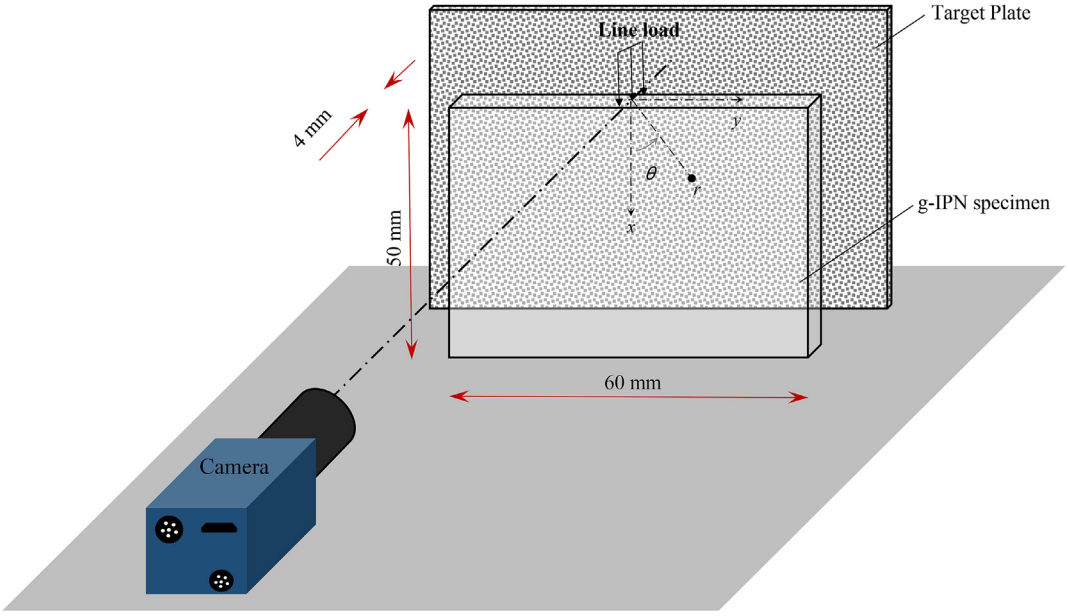

Fig. A1. Experimental setup for edge loading of a g-IPN sheet to evaluate its elasto-optic constant.

An undeformed image of the target plate through the specimen was recorded at no-load condition (1 pixel ~26 μm on the target plane). As the sample was loaded, the deformed images of the target plate were recorded at 0 N, 300 N, 400 N, 600 N and 800 N loads. Two representative speckle patterns, one in the reference (no-load) state and another in the deformed state, are shown in Fig. A2 (a) and (b), respectively. Sufficient care was exercised to obtain a near Gaussian distribution of gray scales for each image in the mid-range of 0–255 (8 bit) scale by adjusting the illumination and the numerical aperture of the lens. The speckles are noticeably distorted in Fig. A2(b) at the top edge of the specimen near the contact area due to deformations and the local stress field. The digitized speckle images (1504 × 1000 pixels) in the deformed state were correlated with the image from the undeformed state using ARAMIS®. A sub-image size of 25 × 25 pixels with an overlap of 20 pixels (i.e., step size of 5 pixels) was used during image correlation. The angular deflection contours in the vertical (x-z) and horizontal (y-z) planes for a compressive load of 800 N for a select composition (80:20 CoP:PU) of grade-1 graft-IPN is shown in Fig. A2 (c) and (d), respectively.

The angular deflections measured in two in-plane orthogonal direction are related to stresses as [4],

$$\phi_{x;y} = \pm C_\sigma \frac{2F}{\pi} \frac{[\cos(2\theta);\ \sin(2\theta)]}{r^2} + C_{x;y} \tag{A1}$$

where C_σ is the elasto-optic constant of the material, F is the applied load, B is the specimen thickness, (r, θ) denote the polar coordinates relative to the loading point, and $C_{x;y}$ denote constants to account for electronic noise and/or rigid motions if any. Linear regression was performed on measured ϕ_x data in the region $1 \le r/B \le 2$ along with angular extent of $-80° \le \theta \le -50°$, $-40° \le \theta \le 40°$, and $50° \le \theta \le 80°$, using Eq. (A1) at each load-step to obtain C_σ which was subsequently averaged. Table A1 shows the elasto-optical constant for all the graft-IPNs synthesized.

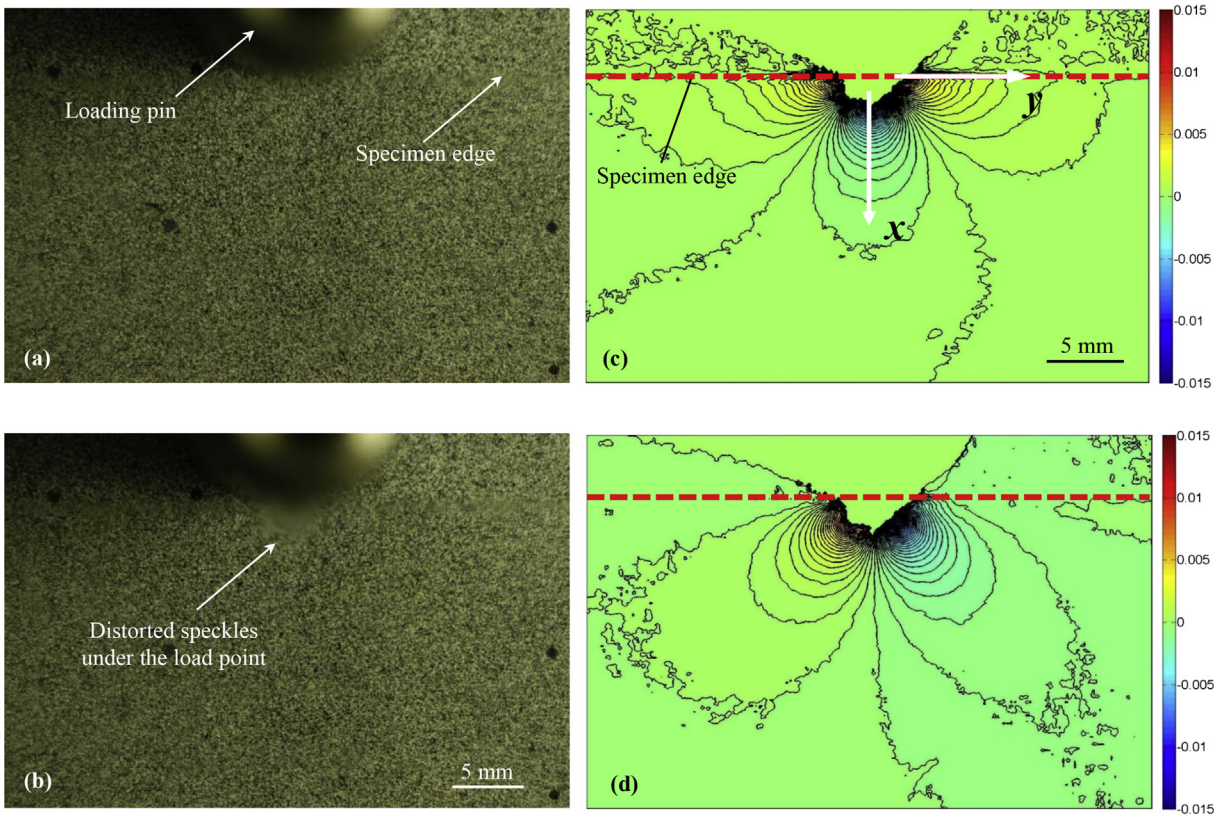

Fig. A2. Left: Speckle images of a select g-IPN (grade-1 80:20 composition) under line-load acting on the specimen edge: (a) undeformed and (b) deformed. Right: Angular deflection contour plots (contour interval = 3×10^{-4} rad) proportional to stress gradients of $(\sigma_x + \sigma_y)$ in the (b) *x*- and, (c) *y*-directions for a select composition (80:20 CoP:PU) of grade-1 graft-IPN subjected to a line-load of 800 N.

Table A1
Elasto-optic constants evaluated for various graft-IPNs.

graft-IPN type	CoP:PU	C_σ(x10^{-10} m^2/N)
650 g mol^{-1} PTMG (Grade-1)	90:10	1.12
	80:20	1.21
	75:25	1.25
	70:30	1.32
	60:40	1.48
1400 g mol^{-1} PTMG (Grade-2)	90:10	1.13
	80:20	1.21
	75:25	1.23
	70:30	1.39
	60:40	1.46

References

[1] R. Ballestero, B.M. Sundaram, H.V. Tippur, M.L. Auad, Sequential graft-interpenetrating polymer networks based on polyurethane and acrylic/ester copolymers, Express Polym. Lett. 10 (3) (2016) 204–215.

[2] P.J. Patel, G.A. Gilde, P.G. Dehmer, J.W. McCauley, Transparent armour, The AMPTIAC Newsletter 4 (3) (2000) Fall.

[3] A. Kobayashi, N. Ohtani, Dynamic fracture in aerospace high polymers, Resins for Aerospace, American Chemical Society, Columbus, OH, 1980, pp. 367–377.

[4] B.M. Sundaram, H.V. Tippur, Dynamic mixed-mode fracture behaviours of PMMA and polycarbonate, Eng. Fract. Mech. 176 (2017) 186–212.

[5] K.C. Jajam, S.A. Bird, M.L. Auad, H.V. Tippur, Tensile, fracture and impact behaviour of transparent Interpenetrating Polymer Networks with polyurethane-poly (methyl methacrylate), Polym. Test. 32 (2013) 899–900.

[6] L.H. Sperling, Interpenetrating Polymer Networks and Related Materials, Plenum Press, New York, 1981.

[7] N. Mignard, N. Okhay, C. Jegat, M. Taha, Facile elaboration of poly-methylmethacrylate/polyurethane interpenetrating networks using Diels-Alder reactions, J. Polym. Res. 20 (2013) 233/1–233/13.

[8] K.C. Frisch, D. Klempner, Advances in Interpenetrating Polymer Networks vols. I-III, Technomic Publishing Co, Lancaster, PA, 1989-1991.

[9] J.R. Millar, Interpenetrating polymer networks. Styreneodivinylbenzene copolymers with two and three interpenetrating networks, and their sulphonates, J. Chem. Soc. (Lond.) (1960) 1311–1317.

[10] L.H. Sperling, V. Mishra, The current status of interpenetrating polymer networks, Polym. Adv. Technol. 7 (1996) 197–208.

[11] L.H. Sperling, D.W. Friedman, Synthesis and mechanical behaviour of interpenetrating polymer networks: poly(ethyl acrylate) and polystyrene, J. Polym. Sci. 2 Polym. Phys. 7 (2) (1969) 425–427.

[12] H.L. Frisch, D. Klempner, K.C. Frisch, A topologically interpenetrating elastomeric network, J. Polym. Sci. B Polym. Lett. 7 (11) (1969) 775–779.

[13] N. Gupta, A.K. Srivastava, Interpenetrating polymer networks: a review on synthesis and properties, Polym. Int. 35 (2) (1994) 109–118.

[14] C. Vasile, A.K. Kulshreshtha, Handbook of Polymer Blends and Composites, Rapra Technology Ltd, Shawbury, 2003.

[15] C.H. Chen, W.J. Chen, M.H. Chen, Y.M. Li, Simultaneous full-interpentrating polymer networks of blocked polyurethane and vinyl ester part I. Synthesis,

swelling ratio, thermal properties and morphology, Polymer 41 (22) (2000) 7961–7967.
[16] L.H. Fan, C.P. Hu, S.K. Ying, Thermal Analysis during the formation of polyurethane and vinyl ester resin interpenetrating polymer networks, Polymer 37 (6) (1996) 975–981.
[17] S.A. Bird, D. Clary, K.C. Jajam, H.V. Tippur, M.L. Auad, Synthesis and characterization of high performance, transparent interpenetrating polymer networks with polyurethane and poly (methyl methacrylate), Polym. Eng. Sci. 53 (4) (2012) 716–723.
[18] L.H. Sperling, Polymeric Multicomponent Materials: an Introduction, Wiley, New York, 1997.
[19] X. Ramis, A. Cadento, J.M. Morancho, J.M. Salla, Polyurathane-unsaturated polyester interpenetrating polymer networks: thermal and dynamic mechanical thermal behaviour, Polymer 42 (23) (2001) 9469–9479.
[20] C.H. Chen, W.J. Chen, M.H. Chen, Y.M. Li, Simultaneous full-interpenetrating polymer networks of blocked polyurethane and vinyl ester Part I. Synthesis, swelling ratio, thermal properties and morphology, Polymer 41 (22) (2000) 7961–7967.
[21] H.F. Lian, P.H. Chun, K.Y. Sheng, Thermal analysis during the formation of polyurethane and vinyl ester resin interpenetrating polymer networks, Polymer 37 (6) (1996) 975–981.
[22] K.H. Hsieh, J.L. Han, Graft interpentrating polymer networks of polyurethane and epoxy. II. Toughening mechanism, J. Polym. Sci. Part B 28 (6) (1990) 783–794.
[23] K.H. Hsieh, J.L. Han, Graft interpentrating polymer networks of polyurethane and epoxy. I. mechanical behaviour, J. Polym. Sci. Part B 28 (5) (1990) 623–630.
[24] K.H. Hsieh, J.L. Han, C.T. Yu, S.C. Fu, Graft interpenetrating polymer networks of urethane-modified bismaleimide and epoxy (I): mechanical behaviour and morphology, Polymer 42 (6) (2001) 2491–2500.
[25] C. Periasamy, H.V. Tippur, Full-field digital gradient sensing method for evaluating stress gradients in transparent solids, Appl. Optic. 51 (12) (2012) 2088–2097.
[26] B.M. Sundaram, H.V. Tippur, Dynamics of crack penetration vs. branching at a weak interface: an experimental study, J. Mech. Phys. Solid. 96 (2016) 312–332.
[27] B.M. Sundaram, H.V. Tippur, Full-field measurement of contact-point and crack-tip deformations in soda-lime glass. Part-I: quasi-static loading, Int. J. Appl. Glass Sci. 9 (1) (2018) 114–122.
[28] B.M. Sundaram, H.V. Tippur, Full-field measurement of contact-point and crack-tip deformations in soda-lime glass. Part-II: stress wave loading, Int. J. Appl. Glass Sci. 9 (1) (2018) 123–136.
[29] B.M. Sundaram, H.V. Tippur, Dynamic fracture of soda-lime glass: a full-field optical investigation of crack initiation, propagation and branching, J. Mech. Phys. Solid. 120 (2018) 132–153.
[30] M. Janssen, J. Zuidema, R.J.H. Wanhill, Fracture Mechanics, Delft Academic Press/VSSD, Delft, 2006.
[31] B.M. Sundaram, H.V. Tippur, Dynamic crack growth normal to an interface in bilayered materials: an experimental study using digital gradient sensing technique, Exp. Mech. 56 (2016) 37–57.